

Stress Relaxation-Induced Colon Tumor Multicellular Spheroid Culture Based on Biomimetic Hydrogel for Nanoenzyme Ferroptosis Sensitization Evaluation

Yi Zhang, Liyi Peng, Ke Hu,* and Ning Gu*

Ferroptosis has recently become a research hotspot, and the induction of tumor cell ferroptosis has emerged as a powerful method for tumor therapy. However, the efficiency of tumor cell ferroptosis induction remains unmet for clinical use, which may be attributed to the large discrepancies between in vitro and in vivo models. To address this issue, in this study, a hydrogel platform with stress relaxation is utilized to develop a multicellular spheroid model of the DLD1 colon cancer cell line through cancer cell self-organization. The spheroids are highly similar to real tumor tissue, and ferroptosis resistance at the transcriptional, protein, and cellular levels. Collaboration of the ferroptosis induction reagent erastin and the nanoenzyme $\text{MnZnFe}_2\text{O}_4$ @PEG-COOH to overcome the ferroptosis resistance of the spheroids is also demonstrated. Taken together, this study demonstrates the effectiveness of the model developed using this hydrogel platform for further mechanistic studies, and for the assessment of novel cancer treatment strategies based on ferroptosis.

levels is of great value in studying ferroptosis mechanisms and evaluating related novel drugs/materials.^[1]

Multicellular spheroids (MCSs) are significantly more representative of the in vivo tissue microenvironment than conventional 2D cultured cells. Thus, MCSs have great potential for cell biological research, tissue engineering, and drug/biomaterial screening.^[2] It has been reported that MCSs have a level of ferroptosis similar to that of in vivo tumors, which is distinct from the ferroptosis of 2D cultured cells.^[3] Therefore, it is important to develop a reliable multicellular sphere model to study ferroptosis in vitro. Nonetheless, the current mainstream strategies for MCSs still have certain limitations, such as high apoptosis rates, limited cellular adaptability, instability, batch-to-batch variability, and poor

mechanical properties of natural hydrogel culture. These limitations are closely related to their failure to provide cells with a microenvironment similar to in vivo models.^[4]

The cellular microenvironment has a critical impact on cell fate. For example, the effect of the mechanical properties of the microenvironment on cells has been a research hotspot in recent years,^[5] among which stress relaxation has been recognized as a decisive factor in cell-extracellular matrix (ECM) interactions and an essential design parameter for biomaterials.^[6] Several experimental and simulation studies have been shown that stress relaxation affects cell proliferation, differentiation, and cytoskeletal organization. Lack of stress relaxation has also been shown to inhibit the proliferation of MCSs.^[7] Based on previous studies on MCSs formation in vitro, we confirmed that the self-organized formation of MCSs could be regulated by adjusting the stress relaxation of the matrix onto which cells grow.^[8]

In this study, we developed a hydrogel platform with adjustable stress relaxation to generate MCSs. This method for generating MCSs mimics the physical microenvironment in vivo by providing cells with a hydrogel matrix with appropriate mechanical and viscoelastic properties, thereby inducing cells to spontaneously form MCSs on the hydrogel through self-organization in a more natural manner. The formation of multicellular structures (spheroids/monolayers) on hydrogels can be regulated by adjusting the stress relaxation of the matrix, thereby providing a new strategy for studying the mechanisms of cellular self-organization and MCS formation. We hypothesized


1. Introduction

The lack of a 3D structure of cells in classical 2D cultures leads to the fact that ferroptosis inducers can easily contact cells by free diffusion, thus amplifying the level of ferroptosis. The vast differences in the in vivo cellular microenvironment also affect the expression of cellular ferroptosis-related markers. Therefore, in vitro construction of cellular models close to in vivo iron death

Y. Zhang
Department of Colorectal Surgery
The First Affiliated Hospital of Nanjing Medical University
Nanjing, Jiangsu 210029, China

L. Peng, K. Hu, N. Gu
Department of Biomedical Engineering
School of Biomedical Engineering and Informatics
Nanjing Medical University
Nanjing, Jiangsu 211103, China
E-mail: kehu@njmu.edu.cn; guning@seu.edu.cn

N. Gu
Jiangsu Key Laboratory for Biomaterials and Devices
School of Biological Science and Medical Engineering
Southeast University
Nanjing, Jiangsu 210096, China

 The ORCID identification number(s) for the author(s) of this article can be found under <https://doi.org/10.1002/adhm.202202009>

DOI: 10.1002/adhm.202202009

that this approach can better mimic some of the specific natural formation processes of solid tumors than encapsulation or micro-porous approaches. Our group has published a series of studies on preparing ferrite nanoenzymes and magnetic induction thermotherapy applications, and proposed a method for developing Mn-Zn ferrite nanomaterials with high magneto-thermal properties.^[9] We evaluated the ability of a series of Mn-Zn ferrite nanoenzymes produced by this method to sensitize ferroptosis using the MCSs obtained from the hydrogel platform, and laid the foundation for the subsequent in vivo study of nanoenzymes sensitizing ferroptosis combined with magnetic induction thermotherapy.

2. Results

2.1. Preparation of Hydrogel Matrix with Tunable Stress Relaxation

The hydrogel platform was prepared by photo-polymerization (405 nm, 10 min) following blending of the cell adhesion part (gelation methacrylate (GelMA)), cell inert part (poly(ethylene glycol) diacrylate (PEGDA)), photoinitiator (lithium phenyl-2, 4, 6-trimethylbenzoylphosphine (LAP)), and crosslinker (methylene bisacrylamide) (Figure 1A; and Figure S1A, Supporting Information). The concentration of GelMA remained constant (10%, w/w) between the MCS condition and monolayer cell (MLC) conditions to provide cells with a consistent adhesion environment.

The MCS hydrogel was prepared with a lower concentration of crosslinker (0.4% in MCSs and 1.2% in MLC hydrogel, w/w) but with a higher concentration of PEGDA (10% in MCS hydrogel and 2% in MLC hydrogel w/w), which resulted in a less dense network in the MCS hydrogel (Figure 1B,C) due to the lower concentration of crosslinker, but a similar elastic modulus between the two types of hydrogel owing to the higher concentration of PEGDA (Figure 1D,E) in MCS hydrogel. Given the lower concentration of crosslinker that resulted in a less dense hydrogel network, the stress relaxation of the MCS culturing hydrogel was significantly higher than that of MLC culturing hydrogel (Figure 1F,G). This result demonstrated that the MCS culturing hydrogel was viscoelastic, whereas the MLC hydrogel was purely elastic.

Next, DLD1 colon cancer cells were seeded on top of both MCS and MLC culturing hydrogels. As expected, cells formed MCS on the MCS culturing hydrogel (Figure 1H–G), and MLC on MLC culturing hydrogel via self-organization (Figure 1K–M).

2.2. Multicellular Tumor Spheroids with Hypoxic Cores Formed on the Hydrogel with Stress Relaxation

Further characterization of the spheroids revealed that while no hypoxia was found in either 2D cultured cells (Figure 2A–C) or MLC (Figure 2D–F) that grown on hydrogel, a compact hypoxic core was observed in each MCS formed on the hydrogel (Figure 2G–I). This indicates that the cell–cell junction is well formed among the cells in the outer layer of the spheroids, which

serves as a barrier to limit the exchange of oxygen, nutrients, and metabolic substances between the cells in the inner layers of spheroids and surrounding cell culture media.

2.3. Multicellular Tumor Spheroid-Growth Reproduced Physiologically Relevant Cell-Microenvironment Interaction

Based on our hypothesis that the material microenvironment we developed is highly similar to the real microenvironment, we reasoned that DLD1 MCSs formed on specific hydrogel subtype should exhibit structural features and molecular markers similar to those of in vivo colon cancer tissues. To test this hypothesis and gain a systematic view of the contribution of genes to the physiological changes that confer malignant phenotype to colon cancer cells, we screened paired human colon adenocarcinoma (COAD) tissues and the adjacent nontumor tissues from three patients using RNA-seq (Figure 3A,B).

To provide insight into biological alterations in colon tumor tissues, we categorized the differentially expressed genes (DEGs) into defined pathways or cellular processes by performing biological function analysis using the Reactome and Gene Ontology (GO) databases. Among the top 20 significantly altered gene clusters, ECM remodeling and cell–matrix interaction related genes appeared with the majority enrichment and statistical significance (Figure 3A). Gene Ontology (GO) analysis further revealed that these genes linked to diverse biological functions including cell communication, ECM disassembly, and cellular component movement (Figure 3B).

We further dissected the gene distribution annotated to the GO term “extracellular matrix disassembly” (GO:0022617) together with “cell-matrix adhesion” (GO:0007160) and found collagen genes, including *COL1A1*, *COL1A2*, adhesion molecules on the cell surface, including *FN1* and integrin family members, as visualized by the heat map (Figure 3C). Moreover, the retrieved DEGs of cell-matrix interaction and ECM between 41 normal and 288 COAD tumor biopsies from The Cancer Genome Atlas (TCGA) Research Network: <http://cancergenome.nih.gov/> were consistent with our RNA-seq analysis results (Figure 3D). Approximately 85% of sporadic or hereditary colorectal tumors are known to be driven by abnormally activated WNT signaling. Thus we further computed the correlation coefficient between architectural structure generation related gene *FN1*, *COL1A1*, and key genes involved in Wnt signaling, including positive regulators *WISP1*, *TCF4*, *CTNNB1* (β -catenin), and negative regulator *AXIN2*.

TCGA data revealed that out of 451 samples COAD tumors displayed a significant FN1-WNT signaling coexpression profile (Figure 3E). These data suggest that colon cancer cells exhibit highly altered focal adhesion dynamics which may contribute to the development and sustainability of the malignant phenotype. In agreement with the in vivo tumor tissue, DLD1 MCSs showed elevated FN1 and COL1A1 (Figure 3D,F,G; and Figure S3, Supporting Information) in both RNA and protein level, and no noticeable difference in E-cadherin and N-cadherin after 7-days culture (Figure 3C,D). These data collectively provide substantial evidence of cell–cell/cell–matrix interactions reconstruction which recapitulates the microenvironment of cells in real tumor tissues.

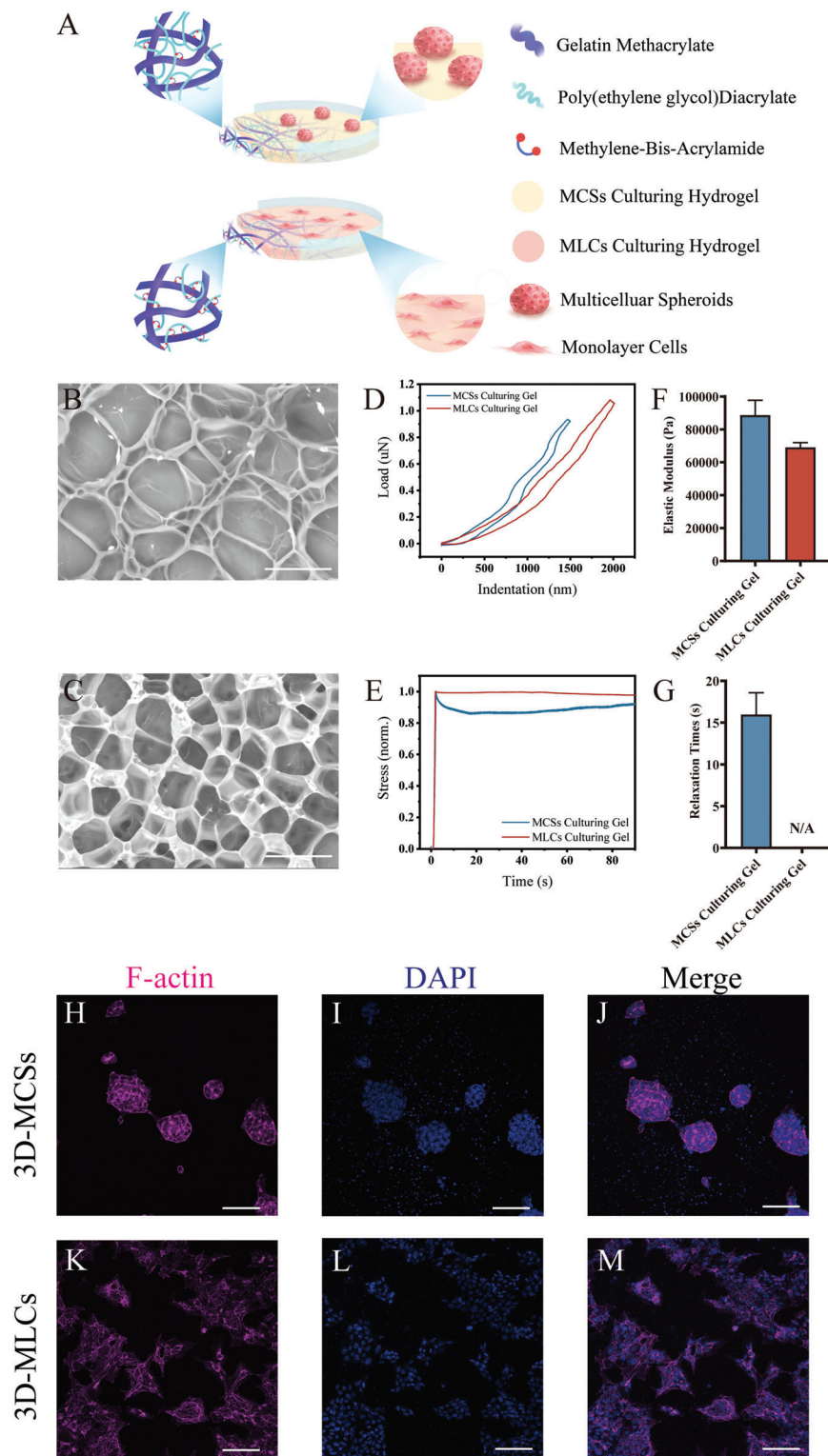


Figure 1. 3D multicellular spheroid culturing hydrogel platform based on stress relaxation. A). Schematic illustration of DLD1 colon cancer cells growing on the viscoelastic/elastic hydrogel. B,C) Cryo-scanning electron microscope images of MCSs culturing hydrogel B) and MLCs culturing hydrogel C). Scale bar: 30 μm . D) Stress-strain curves of MCSs culturing hydrogel and MLCs culturing hydrogel. E) Stress relaxation curves of MCSs culturing hydrogel and MLCs culturing hydrogel. F) Young's modulus of MCSs culturing hydrogel and MLCs culturing hydrogel quantified based on stress-strain curves. G) Stress relaxation of MCSs culturing hydrogel and MLCs culturing hydrogel quantified based on stress relaxation curves. H–M) F-actin H,K), nuclei I,L), and merged images J,M) of cells grown on MCSs culturing hydrogel H–J) and MLCs culturing hydrogel K–M). F-actin: Magenta, DAPI: Blue. Scale bar: 100 μm . Data are presented as mean \pm SD ($n \geq 3$).

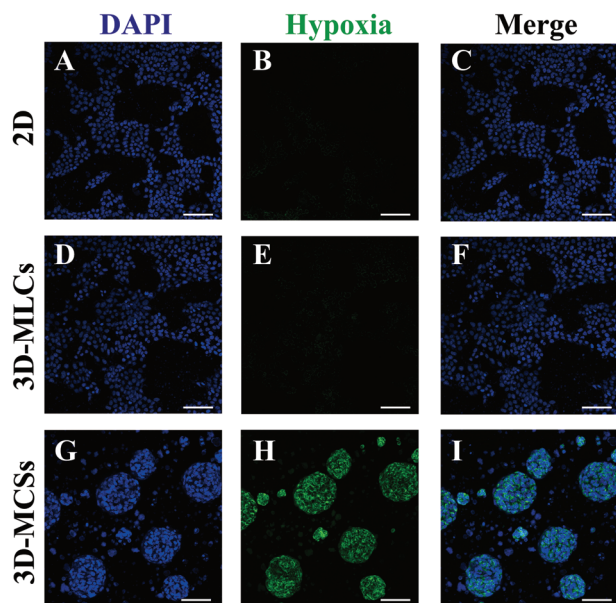


Figure 2. Substantial differences of hypoxia gradients observed on DLD1 colon cancer cells grown on different mechano-microenvironment. A–C) Cells grown on 2D cell culture plate. D–F) Cells grown on MLCs culturing hydrogel. G–I) Cells grown on MCSs culturing hydrogel. A,D,G) Cell nuclei: Blue. B,E,H). Hypoxia marker: Green. C,F,I). Merged images of cell nuclei and hypoxia marker. Scale bar: 100 μ m.

2.4. 3D Spheroids of NRF2-Hyperactivated DLD1 Cells are More Resistant to Ferroptosis

Previous studies have shown that ferroptosis plays an important regulatory role in the occurrence and development of tumors. However, whether ferroptosis involved in colorectal cancer (CRC) development remains unclear. Thus, we analyzed the dataset from CRC patients in CPTCA (Clinical Proteomic Tumor Analysis Consortium) and found that genes related to iron transportation were dysregulated in tumors relative to normal tissues, such as *CP*, *PCPB1*, *PCPB2*, *FTH1*, and *TRFC* (Figure 4A). Tumors showed high expression of ferroptosis suppressor genes including *ACSL3*, *GTF2I*, and *CHERP* (Figure 4A,B). As shown in Figure 4C,D, DLD1-MCSs were significantly more resistant to ferroptosis than 2D cultures. Quantitative polymerase chain reaction (q-PCR) analysis confirmed that the expression of the ferroptosis suppressors *FTH1* and *GPX4* were both upregulated in DLD1-MCSs (Figure 4E,F). It has been reported that NRF2 hyperactivation is necessary for proliferation and anti-ferroptosis in lung tumor spheroids. Western blot analysis (Figure 4G) validated by qPCR (Figure 4H) found that the expression of NRF2 was significantly higher in DLD1-MCSs than in 2D cultured cells, which indicated that CRC tumor cells upregulate oxidative stress defense programs to prevent ferroptosis in spheroids.

2.5. Carboxylated PEG-Coated MnZnFe₂O₄ Nanoenzyme Exhibits High Reactive Oxygen Species Production in 3D Spheroids

Studies have previously reported that increasing cellular reactive oxidative stress (ROS) levels facilitates the ferroptosis activation. Among the many strategies to increase cellular ROS

levels, nanoenzymes are competitive because of their targeting ability and multifunctionality. Our group previously prepared MnZnFe₂O₄ nanomaterials with high magneto-thermal properties and found that this MnZnFe₂O₄ nanoenzyme has peroxidase-like activity and can induce increased cellular ROS levels under acidic conditions. However, different surface-modified nanoenzymes tend to exhibit differences in enzymatic activity. Thus, MnZnFe₂O₄@PEG-COOH, MnZnFe₂O₄@PEG-OCH₃, and MnZnFe₂O₄@PEG-NH₂ were prepared to explore the effect of different surface modifications on the peroxidase-like activity of the materials. Based on the transmission electron microscope (TEM) results, all three materials exhibited good dispersion and stability (Figure 5A–C) with hydrodynamic sizes in the range of 70–100 nm (Figure 5D). MnZnFe₂O₄@PEG-NH₂ has a lower negative potential than MnZnFe₂O₄@PEG-COOH and MnZnFe₂O₄@PEG-OCH₃ (Figure 5E), which is due to the modification of the surface amine groups. We characterized the pH dependence of the three peroxidase-like enzymes (Figure 5F) and showed that all materials exhibited significant peroxidase-like activity in the pH range of 3–6, while almost no activity under physiological conditions, indicating that the nanoparticles can perform peroxide-like functions in the acidic environment of tumors, while they have no peroxidase-like activity in the normal tissue environment. From the reaction time curves and the enzyme concentration dependence (Figure 5G,H), MnZnFe₂O₄@PEG-COOH had the strongest peroxidase-like activity as shown in Figure 5J,K; and Figure S5 (Supporting Information) and a good thermogenesis capacity under an alternating magnetic field (Figure 5I).

2.6. Carboxylated PEG-Coated MnZnFe₂O₄ Nanoenzyme Promotes Erastin-Induced Ferroptosis

To further evaluate the effect of MnZnFe₂O₄@PEG-COOH in promoting erastin-induced ferroptosis through pro-ROS production, we conducted a study on the combined treatment of DLD1-MCSs with erastin and MnZnFe₂O₄@PEG-COOH. Live/dead cell staining showed that MnZnFe₂O₄@PEG-COOH significantly promoted erastin-induced ferroptosis in DLD1-MCSs (Figure 6A), which is consistent with CCK-8 results (Figure S4, Supporting Information). C11-BODIPY is generally used to monitor the flux of lipid ROS in cell membranes, and is assumed to be associated with pro-oxidant activity and excessive PL peroxidation, e.g., during ferroptosis. As shown in Figure 6B; and Figure S6 (Supporting Information), MnZnFe₂O₄@PEG-COOH significantly increased erastin-induced lipid peroxidation in DLD1-MCSs, as indicated by the fluorescence change (red to green). QPCR and western blot analysis further showed that the combination of MnZnFe₂O₄@PEG-COOH significantly decreased the expression of ferroptosis suppressors *FTH1* and *GPX4* in DLD1-MCSs (Figure 6C,D), as well as down-regulated expression of NRF2 (Figure 6E,F).

3. Discussion

The development of advanced 3D tumor cell models,^[10] associated characterization^[11] and validation of cancer therapy methods^[12] have attracted increasing attention. It has been well

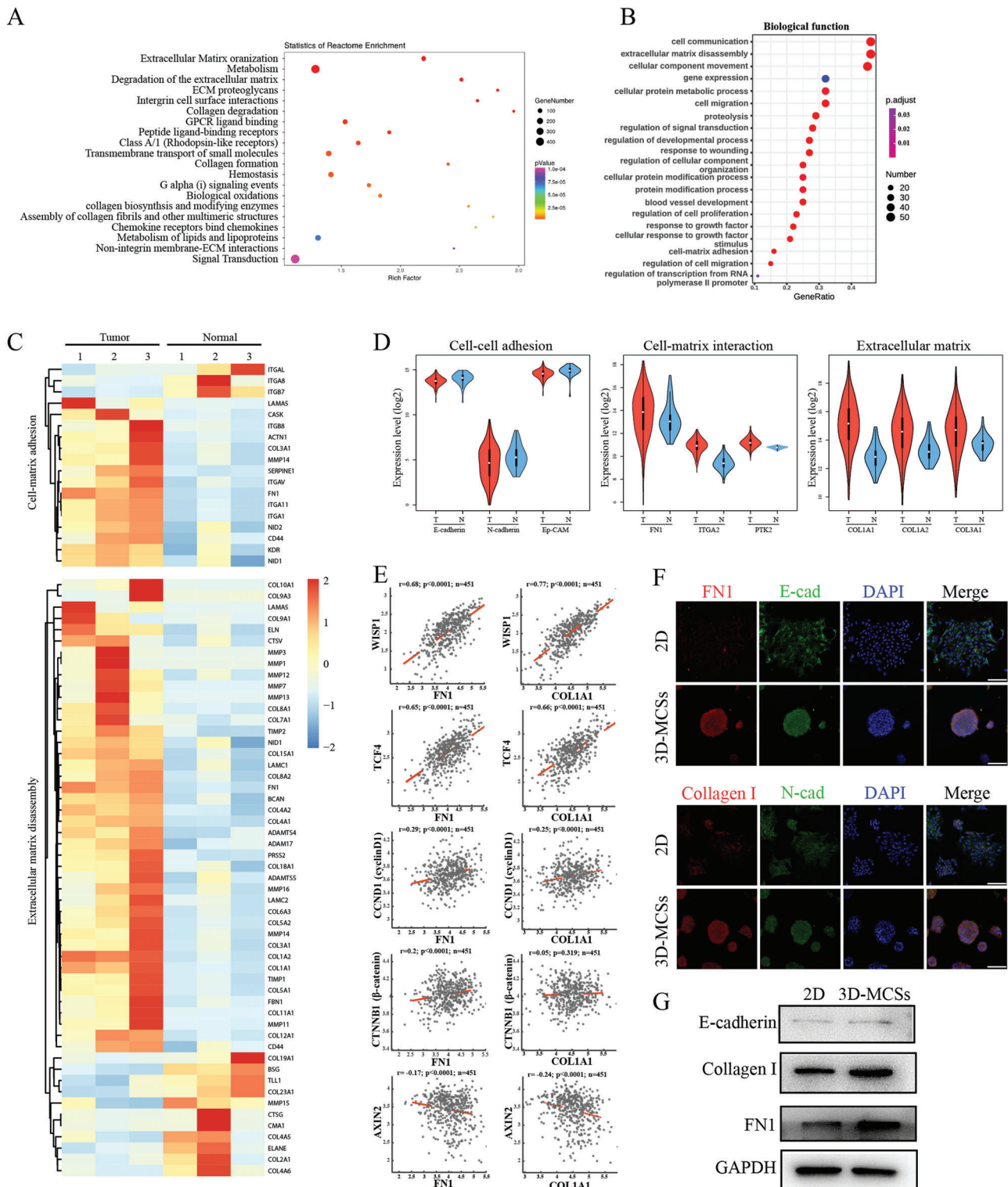


Figure 3. Multicellular spheroids-growth enriched the in vivo molecular phenotype of colon tumor. A) Top enriched Reactome pathways and B) Go terms of DEGs in 3 paired human COAD tissues and the adjacent non-tumor tissues. The size and the color of the dot represent the enriched gene number and range of p values, respectively. C) Heat map representation of genes distribution annotated to the GO term cell–matrix adhesion and extracellular disassembly. D) Violin plot showing the expression distribution of key genes annotated to cell–cell adhesion, cell–matrix interaction and extracellular matrix in 41 normal and 288 tumor tissues. E) Linear regression analysis between the gene expression level of WNT signaling and FN1 or COL1A1 for 451 COAD. F) Representative confocal microscope images of FN1 and COL1 staining (red, with blue DAPI nuclear counterstain) in 2D and MCSs DLD1 cells. Scale bar: 500 μ m. G) Western blot of FN1 and COL1 in 2D and MCSs DLD1 cells.

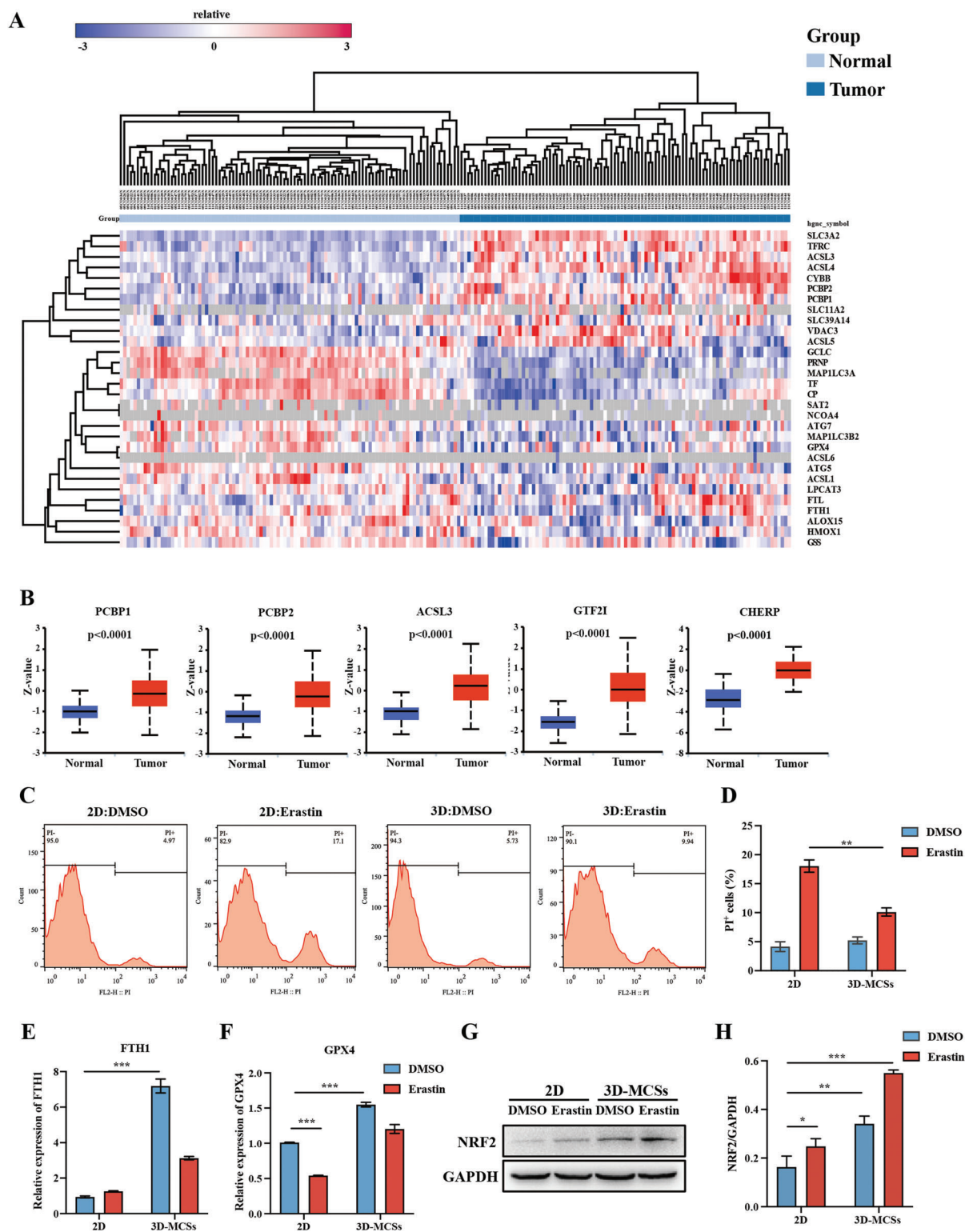
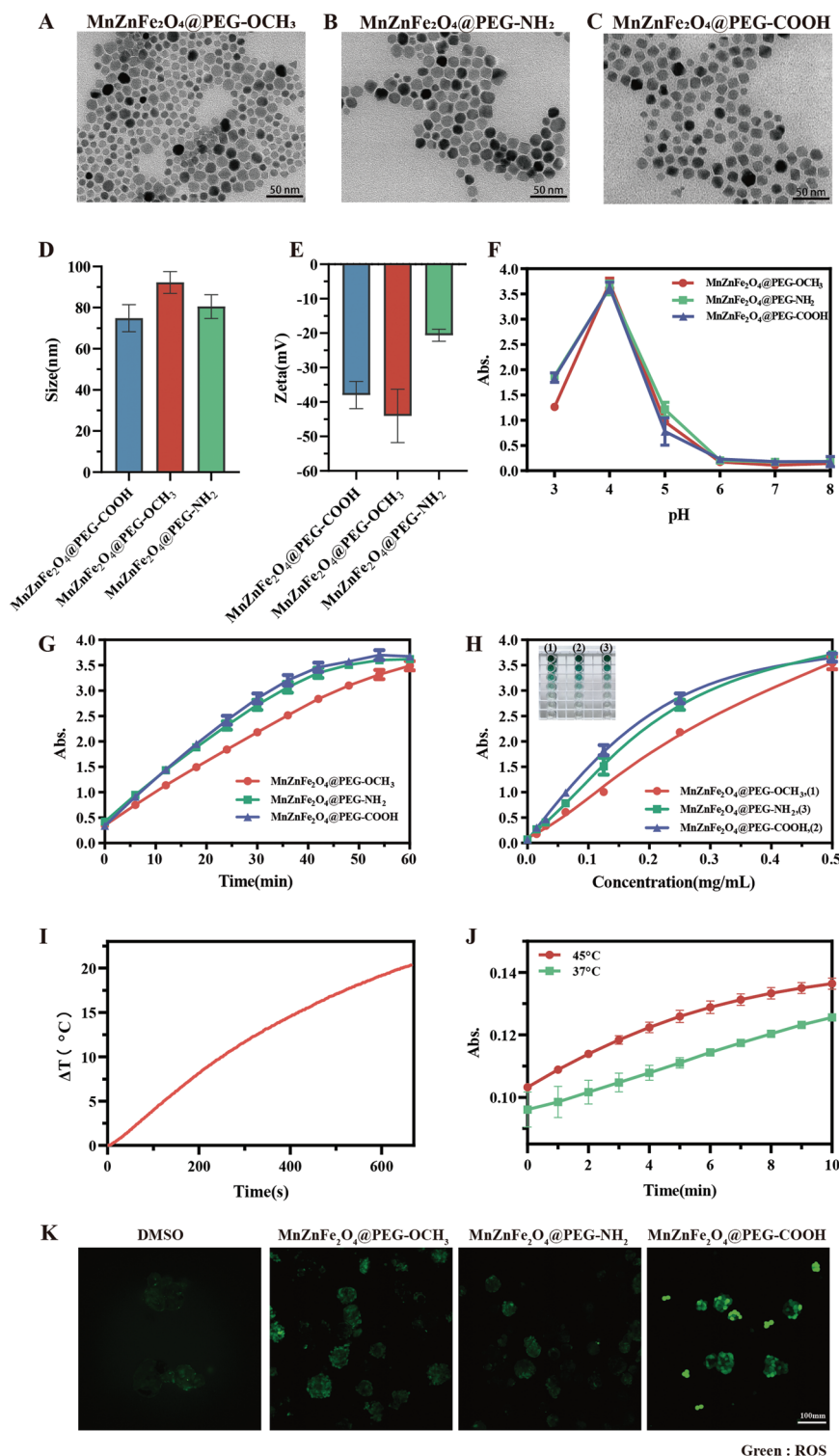
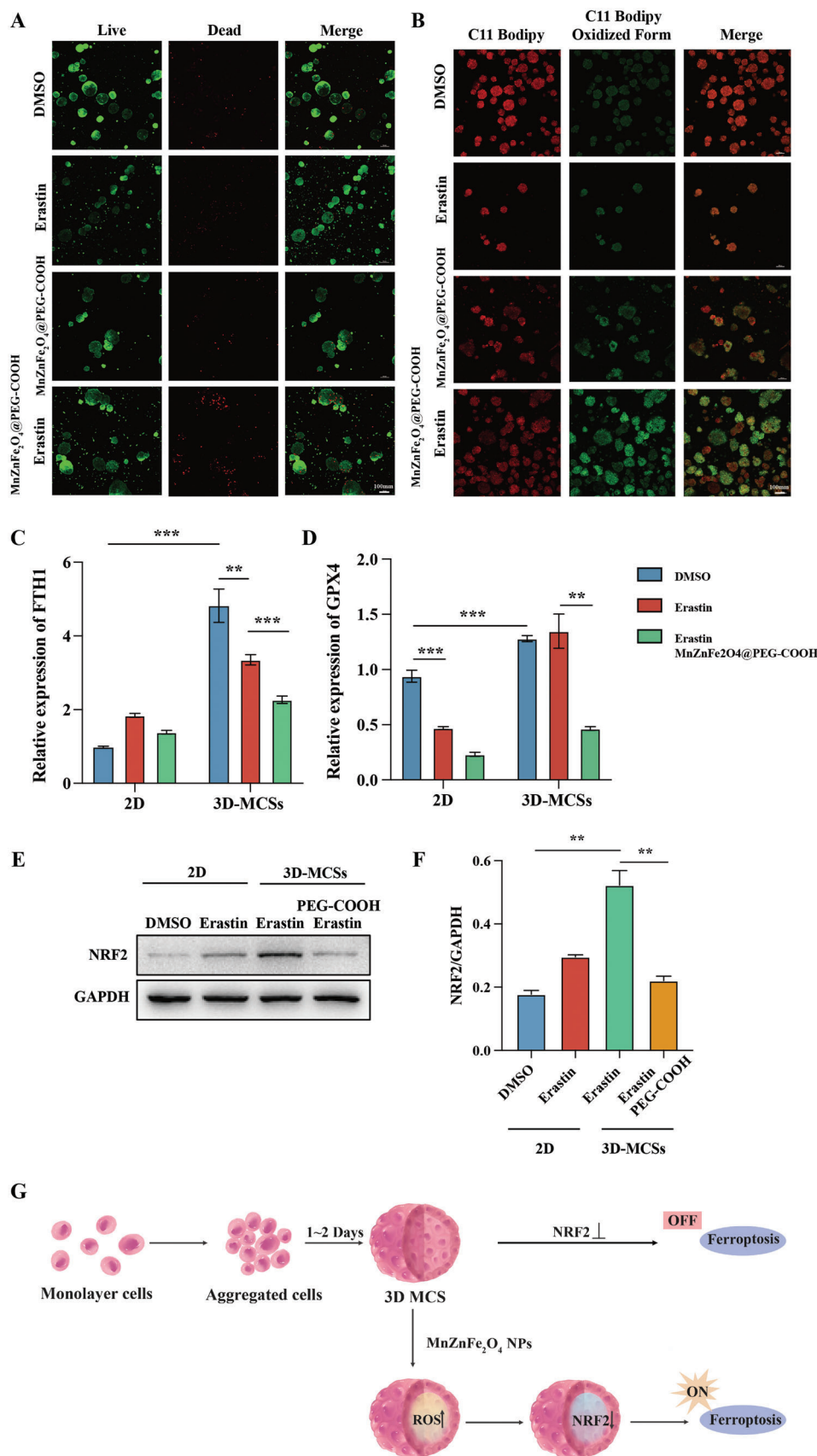


Figure 4. Alteration of ferroptosis-related genes in colorectal cancer and DLD1 MCSs. A) The expression of ferroptosis-related genes in 100 normal and 97 colorectal cancer tissues from CPTCA. B) Box plot showing the expression distribution of significantly altered ferroptosis suppressor genes in CSC dataset from CPTCA. C) Erastin induced ferroptosis in 2D and 3D cultured DLD1 cells was assessed by flow cytometry of PI staining. D) Percentage (%) of dead cells in C). E, F) QPCR analysis of FTH1 and GPX4 in 2D and 3D cultured DLD1 cells with 16 h treatment of erastin. G) Western blot analysis of NRF2 in 2D and 3D cultured DLD1 cells with 16 h treatment of erastin. H) Quantification of western blots presented in G) with ImageJ. Statistical significance is shown over each control. * $p < 0.05$, ** $p < 0.01$, and *** $p < 0.001$ (Student's t -test). Data are presented as mean \pm SD ($n \geq 3$). GAPDH was shown as equal loading for all immunoblots.



Green : ROS

Figure 5. Carboxy PEG modified $\text{MnZnFe}_2\text{O}_4$ has highest POD-like enzymes activity and capacity of ROS generation. A–C) TEM images of methoxy PEG A), Amine PEG B), and carboxy PEG C) modified $\text{MnZnFe}_2\text{O}_4$. D) Hydrodynamic sizes of $\text{MnZnFe}_2\text{O}_4$ with different coating reagent. E). Zeta potential of $\text{MnZnFe}_2\text{O}_4$ with different coating reagent. F) Influence of pH on POD-like enzymes activity of $\text{MnZnFe}_2\text{O}_4$ modified with different coating reagent. G) Time-dependent curves of POD-like enzymes activity of $\text{MnZnFe}_2\text{O}_4$ modified with different coating agents. H). Concentration-dependent curves of POD-like enzymes activity of $\text{MnZnFe}_2\text{O}_4$ modified with different coating agents I). The heating curve of methoxy PEG modified $\text{MnZnFe}_2\text{O}_4$ under alternating magnetic field J). The effect of different temperatures on the POD-like enzymes activity of carboxyl PEG-modified $\text{MnZnFe}_2\text{O}_4$. K) The effect of $\text{MnZnFe}_2\text{O}_4$ modified by different coating agents on the ROS level of tumor multicellular spheroids. Data are presented as mean \pm SD ($n \geq 3$).



recognized the native ECM is of dynamic mechanics with stress relaxation, which significantly regulates different behaviors of cells, such as cancer cell metastasis, ECM sensing, and stemness maintenance of stem cells.^[13] Based on our previous reports that used a hydrogel platform with adjustable stress relaxation to develop self-organization formed colon cancer cell line DLD1 MCSs,^[12c] we demonstrated that formed spheroids were highly similar to the real tumor tissue, which manifested by RNA-seq data

We also showed that formed spheroids with ferroptosis resistance in transcriptional, protein and cell levels, which manifested by the dysregulation of a number of genes that related to iron transportation and ferroptosis suppression, at the same time demonstrated lower ferroptosis ratio compared to 2D cells when being treated with ferroptosis inducer erastin; Formed spheroids could be used to validate the strategy promotion of ferroptosis due to ROS generation from nanoenzymes,

It has been well established that multicellular spheroids mimic real tumor tissue better than 2D cell models.^[14] However, conventional studies normally use nonadherent plates or wells to force cancer cell aggregation by depriving cell–matrix adhesion.^[15] However, this method can generate a substantial number of spheroids relatively rapidly, but deprives the cell–matrix interaction which results in anoikis of cancer cells^[16] and can be a confounding factor when cancer treatment approaches are tested, and cell apoptosis/death rate is used as one of the final readouts. This results in an inability to distinguish whether cells were killed by treatment or by anoikis. We have previously reported the ovarian cancer cell line SKOV-3 and colorectal adenocarcinoma cell line HT-29 MCSs had a higher apoptosis rate in response to the chemotherapeutic reagent doxorubicin when grown in an adhesion deprivation environment compared to those grown on the cell adhesive hydrogel.^[17] In addition to apoptosis, previous reports have highlighted the important role of the matrix in minimizing the susceptibility of cancer cells to ferroptosis. For example, a recent study has indicated that ferroptosis contributes to nonapoptotic cell death resulting from natural matrix interactions deprivation.^[3]

In this study, we confirmed that MCSs grown on the MCS hydrogel matrix are more similar to real tumor tissue than 2D cultured cells regarding the cell–cell/cell–matrix interaction based on RNA-seq data. We reasoned that this is because the mechano-microenvironment cells are being subjected to are more similar to those in vivo. It has been reported that the stress relaxation of soft tissue is in the range of ≈ 10 – 100 s,^[5] which our MCSs hydrogel (≈ 15 s) well falls within (Figure 2E,G). In addition, by eliminating stress relaxation, a significant phenotypic change was observed in the cells, where the formation of spheroids disappeared. Instead, the cells form a sheet-like monolayer (Figure 1K–M). It is still not clear the underlying mechanism of these changes, but previous reports have suggested that several mechanosensi-

tive proteins (e.g., talin, vinculin, etc.) and associated ion channel and transcription factor that regulate cell responses toward surrounding mechano-microenvironment^[18] may contribute to these changes. In the current study, we hypothesized that these factors play important roles in MCSs formation in environments with higher real tumor similarities, and higher resistance to ferroptosis. Notably, contrary to the hypothesis proposed in a previous study that 2D monolayer cells have a higher resistance to ferroptosis,^[3] higher resistance to ferroptosis was observed in MCSs group in our study. Nonetheless, both our study and theirs^[3] confirmed that NRF2 positively correlates with resistance to ferroptosis, but we uniquely observed that NRF2 was upregulated in MCSs. We attribute this difference to the unique mechano-microenvironment that cells were resident in our study.

The other discrepancy between our findings and those of others is that we observed the entry of 80 nm $\text{MnZnFe}_2\text{O}_4$ nanoparticles into the spheroids (Figure S2, Supporting Information), while it has been reported that amount of Au nanoparticles with size larger than 15 nm was minimal.^[19] This could likely because that cells sitting on the outer layer of MCSs first encountered the $\text{MnZnFe}_2\text{O}_4$ nanoparticles, and ferroptosis was initiated at an early stage, therefore resulting the compromising of the integrity of MCSs and subsequent entry of nanoparticles into the core of spheroids.

Despite the advantages of current MCSs model, such as the better mimicry of real tumor tissue (Figure 3) and resistance to ferroptosis (Figure 4) compared to 2D ones, we still recognized the limitation of current MCSs as a surrogate of the patient tumor, which should be addressed in the future studies. First, the supporting matrix is simplified with important ECM protein and/or polysaccharide missing, such laminin, fibronectin, hyaluronan. Second, other stromal cells that comprise the tumor microenvironment, such as immune cells or fibroblast, are not encompassed in the model. In addition, using of primary cancer cells that directly isolated from patient instead of cell line can make this model more capable in predicting the clinical outcome of patient toward treatment.

4. Conclusion

In the present study, we utilized a hydrogel platform with stress relaxation to develop an MCS model of a DLD1 colon cancer cell line formed through cancer cell self-organization. We found that the formed MCSs have high similarity with real tumor tissue validated by RNA-seq, and the MCSs present ferroptosis resistance at the transcriptional, protein, and cell levels. In addition, spheroids can be used to validate the strategy of ferroptosis promotion by the $\text{MnZnFe}_2\text{O}_4$ @PEG-COOH nanoenzyme. Taken together, our results demonstrated the effectiveness of the MCS model developed using this hydrogel platform. Therefore,

Figure 6. $\text{MnZnFe}_2\text{O}_4$ @PEG-COOH enhanced erastin-induced ferroptosis in DLD1 MCSs. A) LIVE/DEAD stain of DLD1 MCSs with treatment of DMSO, Erastin, Erastin combined with $\text{MnZnFe}_2\text{O}_4$ @PEG-COOH. B) Confocal imaging of C11-BODIPY loaded cells with indicated treatment; Red, reduced form of C11-BODIPY; Green, oxidized form of C11-BODIPY. C,D) QPCR analysis of FTH1 and GPX4 in 2D and 3D cultured DLD1 cells with indicated treatment. E) Western blot analysis of NRF2 in 2D and 3D cultured DLD1 cells with indicated treatment. F) Quantification of western blots presented in E) with ImageJ. G) Schematic illustration of the mechanism underlying ferroptosis of MCSs in the presence of $\text{MnZnFe}_2\text{O}_4$ @PEG-COOH. Statistical significance is shown over each control. * $p < 0.05$, ** $p < 0.01$, and *** $p < 0.001$ (Student's *t*-test). Data are presented as mean \pm SD ($n \geq 3$). GAPDH was shown as equal loading for all immunoblots.

this study provides a tool for further mechanistic studies and the assessment of novel cancer treatment strategies based on ferroptosis.

5. Experimental Section

Materials: Polyethylene glycol diacrylate (PEGDA 2000Mw) was purchased from Sigma-Aldrich, and 80% substituted gelatin methacrylate (GelMA) was purchased from Tissue Ink Inc. Lithium phenyl-2,4,6-trimethylbenzoyl phosphate (LAP) was purchased from StemEasy. Three MnZnFe₂O₄ nanoenzymes were purchased from Nanjing NanoEast Biotech Co., Ltd. Unless otherwise stated. All reagents were purchased from Shanghai Aladdin Biochemical Technology Co., Ltd. Erastin was purchased from Selleck Chemicals (Shanghai, China). All the antibodies used in this study were obtained from Abcam. 2',7'-Dichlorofluorescein diacetate (DCFH-DA) was obtained from MCE (HY-D0940). BODIPY 581/591C11 was purchased from Thermo Fisher Scientific (D3861).

Preparation of 3D Cell Culturing Hydrogel: Hydrogels with different mechanical properties were prepared following the protocol report previously.^[12c] Briefly, poly(ethyleneglycol) diacrylate (PEGDA, 2000Mw, sigma), *N,N'*-methylene-bis-acrylamide and gelatin methacryloyl (GelMA, 80% degree of substitution, sigma) that with mass ratio denoted to MCSs culturing hydrogel or MLC culturing hydrogel were added in 1 mL water and dissolved at 50 °C for 2 h. For MCS culture hydrogels, PEGDA (100 mg), *N,N'*-methylenebisacrylamide (0.2% w/w), and GelMA (10 mg) were added, while for monolayer cell (MLC) culture hydrogels, PEGDA (40 mg), *N,N'*-methylenebisacrylamide (1% wt) and GelMA (10 mg) were added. Then LAP (5 mg, sigma) was added in the mixture and dissolved for 5 min. Then the preheated solution was injected into a customized cylindrical mold and irradiated under 405 nm visible light for 10 s for gelation. The Young's modulus and stress relaxation of hydrogel were characterized by Nanoindenter (Optics11, The Piuma, Netherlands). The optical probe (spherical) of the nanoindenter has a tip radius of 24 μm and a stiffness of 40.7 N m⁻¹. The probe was set to press 10 μm in 2 s and unload after holding for 1 s, when measuring Young's modulus. The probe was set to press 15 μm in 5 s and unloaded after holding for 600 s, when measuring stress relaxation. During this procedure, Piuma Nanoindenter's software was implemented to collect data.

Cell Lines and Treatment Conditions: The human colon cancer cell line, DLD1, was cultured in RPMI (Sigma-Aldrich) medium supplemented with 10% FBS (Gibco), 100 U mL⁻¹ penicillin, 100 U mL⁻¹ streptomycin (Sigma-Aldrich), and 1% w/v glutamine (Sigma-Aldrich). For the ferroptosis assay, 2D and 3D-MCSs DLD1 cells were treated with erastin (20 μM, Selleck S7242) or erastin with Mn-Zn ferrite nanoenzymes (200 μg mL⁻¹, Nanjing NanoEast Biotech Co., Ltd) for 24 h. Fluorescence images of the DLD1 cells were captured using a laser scanning confocal microscope (ZEISS LSM T-PMT).

Analysis of TCGA COAD Cohorts: Illumina HiSeqV2 and RSEM normalized RNA-seq gene expression data of normal and COAD tumor samples were retrieved from TCGA.^[20] The Pearson correlation between architectural structure generation-related genes and key genes involved in WNT signaling was computed using the R package Hmisc (<https://CRAN.R-project.org/package=Hmisc>).^[21]

Western Blotting: Briefly, aliquots of 30 μg of lysed proteins from each sample were separated by 10% Sodium Dodecyl Sulfate polyacrylamide gel electrophoresis (SDS-PAGE) and transferred onto polyvinylidene fluoride (PVDF) membranes (Millipore, Bedford, MA). After blocking, the membranes were incubated with the primary antibody overnight at 4 °C, followed by incubation with the secondary antibody for 1 h at room temperature. The blots were visualized by ECL (enhanced chemiluminescence) machine. Each band was quantified using the ImageJ software, and the values were normalized to each loading control band.

ROS and Lipid Peroxidation Staining: The cells were incubated for 30 min at 37 °C with DCFH-DA for ROS measurement or BODIPY 581/591C11 for lipid peroxidation detection. After incubation, cells were digested with trypsin and collected. The ROS and lipid peroxidation lev-

els were imaged using a laser scanning confocal microscope (ZEISS LSM T-PMT).

Quantitative RT-PCR: The cells were collected using 0.5% trypsin. Total RNA was extracted using RNAiso Plus (Takara Bio Inc.; Takara Bio Inc., Japan), and the quantity and quality of RNA were measured using NanoVue Plus (General Electric Company, USA). cDNA was synthesized from 500 ng of RNA using the Prime Script RT Master Mix (RR036A; Takara Bio Inc., Japan) according to the manufacturer's instructions. Quantitative real-time PCR was performed using an ABI 7900 Real-Time PCR System (Thermo Fisher Scientific) with TB Green Premix Ex Taq II (RR820A; Takara Bio Inc., Japan) according to the manufacturer's instructions. Analysis was performed using the 2^{-ΔΔCt} method. Each experiment was performed in triplicate. The primer sequences used were as follows:

	Forward	Reverse
FTTH1	CGACCACTTTGTCAAGCTCA	CCCTGTTGCTGTAGCCAAAT
GPX4	TCCTACGTTTACCTGTCCATGT	GTTTGTGCACTTCCAGTAGTGA
GAPDH	GAGGCAAGACCGAAGTAAACTAC	CCGAAGTGGTTACACGGGAA

Intracellular Detection of Hypoxia: Hypoxia was measured in living MCSs using Image-iT Green Hypoxia Reagent (Thermo Fisher Scientific, I14833), which produces a green fluorescent signal below 5% O₂. Fluorescence images of hypoxia were captured using a laser scanning confocal microscope (ZEISS LSM T-PMT).

Enzyme-Like Activity of Mn-Zn Ferrite Nanozymes and Characterization of Heating Characteristics in Alternating Magnetic Field: MnZnFe₂O₄ nanoparticles were synthesized as follows: Briefly, iron acetylacetonate [Fe(acac)₃, 98%, 2 mmol], zinc acetylacetonate [Zn(acac)₂, 96%, 0.4 mmol], and manganese acetylacetonate [Mn(acac)₂, 97% 0.6 mmol] were added in 20 mL benzyl ether (95%) which contained 9 mmol of oleic acid (90%) and 3 mmol of oleylamine (90%). The mixture was heated to 220 °C at a heating rate of 3.3 °C min⁻¹ and refluxed for 1.5 h under the flow of N₂. Then the mixture was heated to 300 °C at a uniform heating rate in the presence of N₂ flow and maintained at 300 °C for 1.5 h. The final product was washed three times with ethanol (95%) after magnetic separation and finally dispersed in chloroform (99%, 5 mL). Three different coating agents (DSPE-PEG-OCH32000, DSPE-PEG-NH22000, and DSPE-PEG-COOH2000; Nanosoft Polymer, dissolved with chloroform, 5 mL) were added in above mentioned mixture and then 5 mL deionized (DI) water was added gradually. After complete evaporation of chloroform by slow evaporation (70 °C, 30 min), the Mn-Zn ferrite nanozymes became water-soluble. After magnetic separation and 2x ultracentrifugation (100 000 x g), the concentration of Mn-Zn ferrite nanozymes was determined and then stored at 4 °C.

The effect of pH on the peroxidase (POD)-like enzyme activities of MnZnFe₂O₄ modified by different coating agents was tested following the method described below: 100 μL buffers (pH = 4–6: HAC-NaAc; pH = 7–8: PBS) with different pH values (pH = 3, 4, 5, 6, 7, 8), 10 μL MnZnFe₂O₄ (0.25 mg mL⁻¹) modified with different coating agents, 10 μL H₂O₂ (5 mol L⁻¹), 10 μL TMB (5 mg mL⁻¹) were mixed and reacted for 30 min. The absorbance at 652 nm was measured to determine the POD-like enzyme activity.

The concentration-dependent curves of POD enzymes, such as the activity of MnZnFe₂O₄ modified by different coating agents, were tested following the method described below: 100 μL HAC-NaAc buffer (pH = 4), 10 μL MnZnFe₂O₄ with different concentrations (0, 0.015, 0.03, 0.0625, 0.125, 0.25, 0.5 mg mL⁻¹) and modified with different coating agents, 10 μL H₂O₂ (5 mol L⁻¹), 10 μL TMB (5 mg mL⁻¹) were mixed and reacted for 30 min. The absorbance at 652 nm was measured to determine the POD enzyme-like activity.

The time-dependent curves of the POD enzymes, such as the activity of MnZnFe₂O₄ modified with different coatings, were tested following the method described below: PBS buffer pH = 7, 10 μL MnZnFe₂O₄ (0.25 mg mL⁻¹) modified with different coating agents, 10 μL H₂O₂ (5 mol L⁻¹), 10 μL TMB (5 mg mL⁻¹) were mixed and reacted for 30 min. The ab-

sorbance at 652 nm at different reaction time points was measured to determine POD enzyme-like activity.

The effects of different temperatures on the activity of carboxyPEG-modified $\text{MnZnFe}_2\text{O}_4$ POD-like POD enzymes were tested according to the following methods: 100 μL HAc-NaAc buffer ($\text{pH} = 5.2$), 10 μL (0.25 mg mL^{-1}) carboxylPEG-modified $\text{MnZnFe}_2\text{O}_4$, 10 μL H_2O_2 (5 mol L^{-1}), 10 μL TMB (5 mg mL^{-1}); the absorbance at 652 nm was tested at different reaction time points at 37 and 45 $^\circ\text{C}$, respectively.

The heat generation of the $\text{MnZnFe}_2\text{O}_4$ NPs (1.0 mg Fe mL^{-1} , 1 mL) was carried out using a moderate/high radio frequency alternating magnetic field (Shuangping SPG-06-III frequency: 390 KHz; current: 12 A).

Statistics: Data were tested using unpaired *t*-test when two groups were compared and was tested by analysis of variance (ANOVA) and Tukey post hoc test when more than two groups were compared. Statistical analysis was performed using R (version 3.6.1) and GraphPad Prism (version 8.2.1). For all experiments with error bars, standard deviation (SD) was calculated and *p* values represent mean \pm SD. Presented data are an average of at least three independent experiments ($n \geq 3$) or representative of independent experiments.

Supporting Information

Supporting Information is available from the Wiley Online Library or from the author.

Acknowledgements

This work was supported by the National Key Research and Development Program of China (No. 2021YFA1201301) and the Talent Introduction Foundation of Nanjing Medical University (No. 2017RC07). The authors thank Zhaobin Guo from Johns Hopkins University for editing the manuscript and Tingting Yu from Nanjing Medical University for discussion of this work.

Conflict of Interest

The authors declare no conflict of interest.

Author Contributions

Y.Z.: Conceptualization, Resources, Methodology, Investigation, Formal analysis, Writing—original draft. L.P.: Investigation. K.H.: Conceptualization, Funding acquisition, Formal analysis, Writing—original draft, Resources, Methodology, Investigation, Formal analysis. N.G.: Supervision, Funding acquisition, Project administration.

Data Availability Statement

The data that support the findings of this study are available from the corresponding author upon reasonable request.

Keywords

3D cell cultures, ferroptosis, hydrogels, multicellular spheroids, nanoenzymes

Received: August 8, 2022

Revised: October 9, 2022

Published online: November 1, 2022

- [1] X. Chen, R. Kang, G. Kroemer, D. Tang, *J. Exp. Med.* **2021**, 218, e20210518.
- [2] C. M. Madl, S. C. Heilshorn, H. M. Blau, *Nature* **2018**, 557, 335.
- [3] N. Takahashi, P. Cho, L. M. Selfors, H. J. Kuiken, R. Kaul, T. Fujiwara, I. S. Harris, Z. Zhang, S. P. Gygi, J. S. Brugge, *Mol. Cell* **2020**, 80, 828.

- [4] a) J. Dang, S. K. Tiwari, G. Lichinchi, Y. Qin, V. S. Patil, A. M. Eroshkin, T. M. Rana, *Cell Stem Cell* **2016**, 19, 258; b) Y. Li, E. Kumacheva, *Sci. Adv.* **2018**, 4, eaas8998.
- [5] O. Chaudhuri, J. Cooper-White, P. A. Janmey, D. J. Mooney, V. B. Shenoy, *Nature* **2020**, 584, 535.
- [6] O. Chaudhuri, L. Gu, D. Klumpers, M. Darnell, S. A. Bencherif, J. C. Weaver, N. Huebsch, H.-p. Lee, E. Lippens, G. N. Duda, *Nat. Mater.* **2016**, 15, 326.
- [7] a) G. Helmlinger, P. A. Netti, H. C. Lichtenbeld, R. J. Melder, R. K. Jain, *Nat. Biotechnol.* **1997**, 15, 778; b) H. Yan, D. Ramirez-Guerrero, J. Lowengrub, M. Wu, *PLoS Comput. Biol.* **2021**, 17, e1009701.
- [8] a) X. Han, S. Tang, L. Wang, X. Xu, R. Yan, S. Yan, Z. Guo, K. Hu, T. Yu, M. Li, *Int. J. Nanomed.* **2021**, 16, 5101; b) M. Zhang, S. Yan, X. Xu, T. Yu, Z. Guo, M. Ma, Y. Zhang, Z. Gu, Y. Feng, C. Du, *Biomaterials* **2021**, 270, 120687.
- [9] a) J. Xie, C. Yan, Y. Yan, L. Chen, L. Song, F. Zang, Y. An, G. Teng, N. Gu, Y. Zhang, *Nanoscale* **2016**, 8, 16902; b) J. Xie, C. Yan, Y. Zhang, N. Gu, *Chem. Mater.* **2013**, 25, 3702; c) J. Xie, Y. Zhang, C. Yan, L. Song, S. Wen, F. Zang, G. Chen, Q. Ding, C. Yan, N. Gu, *Biomaterials* **2014**, 35, 9126.
- [10] a) V. L. Silvestri, E. Henriot, R. M. Linville, A. D. Wong, P. C. Searson, A. J. Ewald, *Cancer Res.* **2020**, 80, 4288; b) Z. Zhou, K. Van der Jeught, Y. Fang, T. Yu, Y. Li, Z. Ao, S. Liu, L. Zhang, Y. Yang, H. Eyvani, *Nat. Biomed. Eng.* **2021**, 5, 1320.
- [11] a) Z. Guo, C. T. Yang, C. C. Chien, L. A. Selth, P. O. Bagnaninchi, B. Thierry, *Small Methods* **2022**, 6, 2200471; b) H.-Y. Liao, C.-C. Huang, S.-C. Chao, C.-P. Chiang, B.-H. Tang, S.-P. Lee, J.-K. Wang, *Biosensors* **2022**, 12, 304.
- [12] a) Z. Guo, C. T. Yang, M. F. Maritz, H. Wu, P. Wilson, M. E. Warkiani, C. C. Chien, I. Kempson, A. R. Aref, B. Thierry, *Adv. Mater. Technol.* **2019**, 4, 1800726; b) T. Yu, Y. Hu, G. Feng, K. Hu, *Adv. Ther.* **2020**, 3, 1900195; c) Y. Zhang, Z. b. Guo, Y. m. Nie, G. p. Feng, M. j. Deng, Y. m. Hu, H. j. Zhang, Y. y. Zhao, Y. w. Feng, T. t. Yu, *Macromol. Biosci.* **2022**, 22, 2100498.
- [13] a) Y. Ma, T. Han, Q. Yang, J. Wang, B. Feng, Y. Jia, Z. Wei, F. Xu, *Adv. Funct. Mater.* **2021**, 31, 2100848; b) C. M. Madl, B. L. LeSavage, R. E. Dewi, C. B. Dinh, R. S. Stowers, M. Khariton, K. J. Lampe, D. Nguyen, O. Chaudhuri, A. Enejder, *Nat. Mater.* **2017**, 16, 1233; c) S. Tang, H. Ma, H. C. Tu, H. R. Wang, P. C. Lin, K. S. Anseth, *Adv. Sci.* **2018**, 5, 1800638; d) M. Wang, B. Cheng, Y. Yang, H. Liu, G. Huang, L. Han, F. Li, F. Xu, *Nano Lett.* **2019**, 19, 5949.
- [14] a) L. A. Kunz-Schughart, M. Kreutz, R. Kneuchel, *Int. J. Exp. Pathol.* **1998**, 79, 1; b) R. Z. Lin, H. Y. Chang, *Biotechnol. J.* **2008**, 3, 1172.
- [15] a) E. C. Costa, D. de Melo-Diogo, A. F. Moreira, M. P. Carvalho, I. J. Correia, *Biotechnol. J.* **2018**, 13, 1700417; b) E. Fennema, N. Rivron, J. Rouwkema, C. van Blitterswijk, J. De Boer, *Trends Biotechnol.* **2013**, 31, 108.
- [16] a) C. L. Chaffer, B. P. San Juan, E. Lim, R. A. Weinberg, *Cancer Metastasis Rev.* **2016**, 35, 645; b) J. Y. Kim, N. Lee, Y.-J. Kim, Y. Cho, H. An, E. Oh, T.-M. Cho, D. Sung, J. H. Seo, *Cancer Lett.* **2017**, 386, 151.
- [17] S. Tang, K. Hu, J. Sun, Y. Li, Z. Guo, M. Liu, Q. Liu, F. Zhang, N. Gu, *ACS Appl. Mater. Interfaces* **2017**, 9, 10446.
- [18] a) J. D. Humphrey, E. R. Dufresne, M. A. Schwartz, *Nat. Rev. Mol. Cell Biol.* **2014**, 15, 802; b) P. A. Janmey, D. A. Fletcher, C. A. Reinhart-King, *Physiol. Rev.* **2020**, 100, 695; c) J. Z. Kechagia, J. Ivaska, P. Roca-Cusachs, *Nat. Rev. Mol. Cell Biol.* **2019**, 20, 457.
- [19] K. Huang, H. Ma, J. Liu, S. Huo, A. Kumar, T. Wei, X. Zhang, S. Jin, Y. Gan, P. C. Wang, *ACS Nano* **2012**, 6, 4483.
- [20] J. Liu, T. Lichtenberg, K. A. Hoadley, L. M. Poisson, A. J. Lazar, A. D. Cherniack, A. J. Kovatich, C. C. Benz, D. A. Levine, A. V. Lee, *Cell* **2018**, 173, 400.
- [21] G. Ambrose, T.-t. Yu, B. Zhang, M. Kacal, Y. Hao, A. L. Queiroz, A. T. Ouchida, C. Lindskog, E. Norberg, H. Vakifahmetoglu-Norberg, *Br. J. Cancer* **2020**, 123, 1164.